Statistical mechanics of magnetic bubble arrays. II. Observations of two-dimensional melting

R. Seshadri and R. M. Westervelt
Division of Applied Sciences and Department of Physics, Harvard University, Cambridge, Massachusetts 02138
(Received 5 March 1992)

We report observations of a continuous hexatic-to-liquid melting transition as a function of density in two-dimensional magnetic bubble arrays in garnet films. Bubble arrays can be directly viewed and their motion recorded. The hexatic with orientational order undergoes a phase transition to form an isotropic liquid when dislocations unbind into disclinations. Melting occurs via the formation of progressively larger transient defect clusters that gradually percolate into one another, and eventually span the system destroying orientational order. Observations made in a linear magnetic-field gradient indicate that the transition is continuous. Defect dynamics, concentrations, and mobilities characterize the melting process. At the transition bubble motion goes from constrained in the hexatic to diffusive in the liquid. The transition is described well by a phenomenological criterion: melting occurs when the root mean square of the difference between displacements of adjacent bubbles is $\sim 10\%$ of the average lattice spacing. At higher bubble densities, away from the transition, we observe a hexatic glass characterized by extended orientational order, very few immobile dislocations, and short-range translational order limited by substrate roughness.

I. INTRODUCTION

The nature of the melting transition that transforms a crystalline two-dimensional solid, with long-range orientational order and quasi-long-range translational order, into an isotropic liquid has been a subject of considerable interest and controversy over the past few decades.[1-3] Two-dimensional lattices with continuous symmetries do not display long-range translational order at finite temperatures, because these systems are susceptible to long-wavelength phonons. This result, originally postulated by Peierls and Landau, was derived rigorously by Mermin,[4] who also showed that long-range orientational order can be present despite the absence of long-range translational order. However, in a broad class of two-dimensional systems with two-dimensional order parameters and Abelian symmetry (including two-dimensional solids, superfluids, and x-y magnets), quasi-long-range translational order in which translational correlations decay algebraically is observed at finite temperatures.

Building on the ideas of Kosterlitz and Thouless,[5] Halperin and Nelson have proposed that melting in two-dimensional solids is a continuous two-stage transition driven by topological defects: dislocations and disclinations.[6-8] The crystalline phase is characterized by quasi-long-range translational order and long-range orientational order. The first stage of the melting transition occurs when dislocation pairs unbind to form a hexatic phase with short-range translational order and quasi-long-range orientational order. The second stage occurs when disclination pairs making up dislocations unbind, destroying orientational order to form a liquid. Young[9] independently studied the crystal-to-hexatic transition via dislocation pair unbinding. Other theoretical works[10-14] propose that two-dimensional melting is a single first-order transition as in three dimensions. The nature of two-dimensional melting has been studied in numerical simulations,[1,2,15,16] and experiments on a variety of physical systems including binary arrays of hard spheres,[17] polystyrene colloids,[18-21] holes in ferrofluids,[22] liquid crystals,[1,2] electrons on Helium,[1,2] and noble gases physisorbed on substrates.[1,2]

If present, substrate roughness acts to destroy quasi-long-range translational order in two-dimensional solids. Larking and Ovchinnikov[23] have shown that translational order is short-range in two-dimensional flux lattices in the presence of weak collective pinning due to random disorder. Recently, Chudnovsky[24] extended this work to show that orientational order is preserved despite the absence of translational order. He also suggested that the hexatic-to-crystal transition is absent in two-dimensional systems with substrate roughness, so that a hexatic glass rather than a crystalline solid is the most ordered state. Related theoretical work using a physically relevant model for the microscopic substrate roughness has been done by Bouchaud, Mezard, and Yedidia.[25] In both of these theoretical approaches, translational order in the predicted hexatic glasses is limited by substrate roughness rather than by dislocations as in a Halperin-Nelson hexatic. Nelson, Rubinstein, and Spaepen showed that frozen-in dislocations can produce a glassy Halperin-Nelson hexatic phase analogous to the equilibrium hexatic originally proposed.[17] A hexatic vortex glass has been imaged in disordered high-T_c superconductors, although dynamic measurements have not been reported.[26,27] Experimentally it can be difficult to separate the effects of substrate roughness from the effects of dislocations and residual strain fields.

In this paper we present experimental observations of a continuous hexatic-to-liquid melting transition near equilibrium driven by topological defects in agreement with the equilibrium Halperin-Nelson theory.[6-9] Away from

the transition we describe observations of glassy hexatics associated with microscopic substrate roughness and nonequilibrium dislocations, related to those described by Chudnovsky,[24] by Bouchaud, Mezard, and Yedidia[25] and by Nelson, Rubinstein and Spaepen.[17] An early account of this work appeared in Ref. 28.

Magnetic bubble arrays in thin garnet films are an easily accessible system in which to study two-dimensional melting. Material properties of magnetic garnet films are well understood, and bubble domains in these films have been thoroughly investigated for device purposes.[30,31] As described in part I (Ref. 29), the motion of magnetic bubble arrays can be visualized, recorded, and studied in detail. Using Voronoi constructions topological defects can be unambiguously identified and tracked. These advantages are usually associated with numerical simulations rather than experiments. However, numerical simulations have severe constraints imposed by available computational time including relatively small numbers of particles, periodic boundary conditions, and short equilibration times. Our experiments are conducted on a real physical system without built-in assumptions. By using polycrystalline bubble arrays, we achieve boundary conditions for individual grains that minimize residual stress and make equilibration possible in experimentally accessible times.

This paper is organized as follows. Section II describes the experimental methods. Section III presents detailed observations of the melting process and the related phases via the visualization of topological defects. Section IV presents statistical descriptions of the phase transition via correlation functions. Section V uses measurements of the bubble diffusion constant and defect dynamics to explore the process of equilibration. Section VI describes the behavior of defect concentrations and distributions in the hexatic glass and the hexatic-to-liquid transition. In Sec. VII a phenomenological description derived from measurements of the bubble displacements and lattice spacing is used to describe the melting transition. In Sec. VIII we describe an experiment which shows that the hexatic-to-liquid phase transition is continuous. In Sec. IX we summarize our findings, and make comparisons with theory and numerical simulations.

II. EXPERIMENTAL METHODS

Magnetic bubbles are cylindrical domains of reversed magnetization in thin magnetic films, which have been extensively studied in the past.[30,31] In this work we use thin films of bismuth-substituted-iron-garnet developed for magneto-optic applications by the Airtron Division of Litton Industries.[32] The properties of these samples are described in detail in Ref. 29. The film is grown on a transparent substrate of nonmagnetic garnet with matched lattice constant to a thickness 7.8 μm, with a strong uniaxial anisotropy perpendicular to the plane of the film. The measured magnetization and Curie temperature are $4\pi M = 190$ G and $T_{\text{curie}} = 170\,^{\circ}\text{C}$. Bubble domain walls in this film are thin (~ 0.1 μm) compared to the domain sizes (~ 10 μm), and the motion of bubbles within the film is two dimensional. Patterns of bubbles can be viewed directly in real space and time via the Faraday rotation of polarized light, and recorded using optical microscopy and digital imaging techniques. Grey scale images of bubble arrays are digitally processed to find the bubble centers, which are indicated in the processed data below by dots. Voronoi constructions on the array of bubble centers were used to determine the coordination of each bubble and to locate topological defects in the array. In the processed images below, fivefold disclinations are indicated by black squares and sevenfold disclinations by black circles; rarer fourfold and eightfold disclinations are indicated by open squares and circles, respectively. Details of the experimental methods used to record and analyze images, and extensive descriptions of the topological structure and thermalization of the system are given in Ref. 29.

Magnetic bubble arrays are created by briefly applying a strong in-plane magnetic field ($H = 2.5$ kG) which overcomes the uniaxial anisotropy and rotates the magnetization into the plane of the sample; when the in-plane field is removed, a disordered sea of bubbles is created.[29] The sample is then placed under the microscope in a perpendicular magnetic field with two components: a time-dependent dc bias magnetic field H_B which opposes the bubble magnetization, and a sinusoidal ac magnetic field with variable amplitude H_{ac} and frequency 40 Hz. Polycrystalline bubble arrays are created by annealing the disordered sea of bubbles in superimposed dc and ac magnetic fields. Experiments on the melting of bubble arrays described below are done within single crystallites of $\sim 12\,000$ bubbles within a polycrystalline array. The applied perpendicular dc bias field H_B is used to adjust the areal density ρ of the bubbles by destroying bubbles at random locations, as described below. Isolated bubbles collapse at a well-defined value H_{CO} of the applied field H_B, which for our samples is $H_{CO} = 103$ Oe in the absence of the ac field. Over the range of applied fields used in this experiment ($85\text{ Oe} < H_B < 95\text{ Oe}$) the areal density of the bubbles decreases with H_B via bubble collapse, but the bubble radius does not vary appreciably, as described for regime 3 in Ref. 29. The applied ac field H_{ac} is used to overcome coercive friction and to create random bubble motion which stimulates thermal motion, described in detail in Ref. 29. The applied ac field produces a slight breathing motion of the bubble radius, which couples to the underlying microscopic substrate roughness to produce Brownian motion in the position of the bubbles corresponding to an effective temperature.[29] For the work described below, the amplitude of the ac field was fixed at $H_{\text{ac}} = 6.6$ Oe peak to peak.

The experiments on two-dimensional melting are performed by decreasing the areal bubble density ρ from $\sim 4000\ \text{mm}^{-2}$ to $\sim 500\ \text{mm}^{-2}$ by incrementing the bias field H_B in small steps from 85 to 95 Oe. The steps in field were adjusted to give an approximately steady decrease in density. Figure 1(a) plots the measured density ρ versus H_B from one experimental run. The corresponding increase in the average lattice spacing measured using Voronoi constructions on the bubbles centers[29] is shown

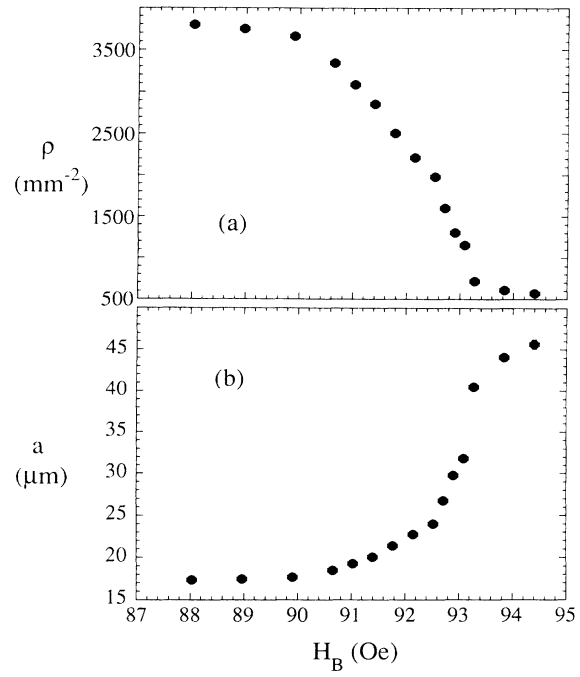

FIG. 1. (a) Bubble density ρ averaged over several images spanning a large area vs applied bias magnetic field H_B, for one experimental run of the melting experiment. Note the bubble radius r does not change over the range of H_B used. (b) Average lattice spacing a determined from Voronoi constructions vs applied field H_B.

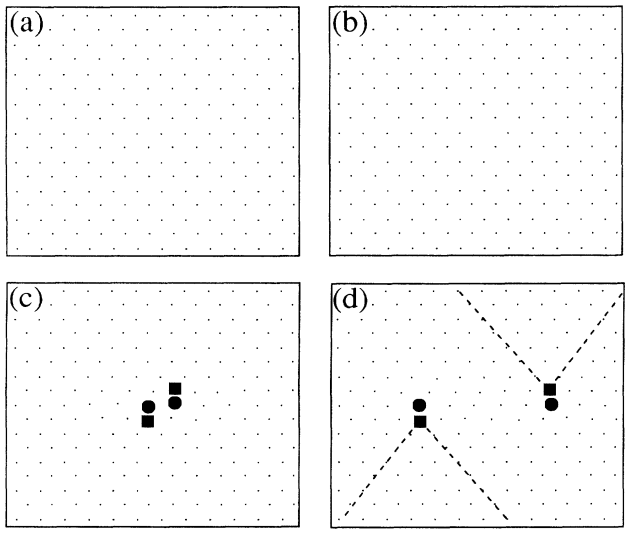

FIG. 2. Schematic diagram illustrating the introduction of dislocations when bubbles collapse following a bias field increment. (a) Perfect hexagonal array at bias field H_B. (b) When H_B is incremented to $H_B+\Delta H_B$ bubbles collapse creating vacancies such as the one shown at the center of the array. (c) Vacancies relax into dislocations. Two dislocations are shown here: black squares and circles represent five- and sevenfold disclinations, respectively, and a five-seven pair corresponds to a dislocation. (d) Dislocations then equilibrate with each other and with the grain boundary, primarily via glide. Dashed lines illustrate the extra rows associated with each dislocation, and the glide direction is the lattice direction with no extra rows.

in Fig. 1(b). A reduction in the bubble density ρ following an increment in bias field occurs via the collapse of bubbles at randomly located positions in the array where the total field exceeds the bubble collapse field H_{CO}. Each bubble that collapses leaves a vacancy in the array which quickly relaxes into two or more dislocations. This process is illustrated schematically in Fig. 2. When the array in Fig. 2(a) is subject to a small increment in H_B, a bubble collapses creating a vacancy in the center of Fig. 2(b). Neighboring bubbles move in to fill the vacancy, which relaxes into a pair of dislocations, as shown in Fig. 2(c). Each dislocation is composed of a bound fivefold and sevenfold disclination pair; fivefold and sevenfold disclinations are indicated in Fig. 2 by black squares and circles, respectively. These dislocations typically glide apart, and move separately, as shown in Fig. 2(d). The two extra rows of bubbles corresponding to the presence of each dislocation are indicated by dashed lines.

Therefore, in this experiment each reduction in bubble density ρ produces dislocations distributed over the array. In order to permit these dislocations to equilibrate with each other and with the grain boundary as described below, the array is annealed after each step in H_B for 30 min in the applied ac field $H_{ac}=6.6$ Oe peak to peak. Video images of the dynamics of the array are recorded during this period. At the end of the annealing period the amplitude of the ac field is gradually reduced to zero, digital images of the array are recorded, and then the amplitude of the ac field is slowly turned up again to its previous value. Images are recorded without an ac field to minimize the uncertainty in bubble locations.

Boundary conditions for a crystalline grain in the polycrystalline bubble array make equilibration possible in experimentally accessible time scales. The polycrystalline array minimizes unwanted external stresses on the crystallite. The grain boundary also serves as a reservoir of dislocations surrounding the crystallite. Any point in the crystallite can be reached by a dislocation of any orientation from the grain boundary via dislocation glide. The slower process of dislocation climb is not necessary to attain equilibrium for these boundary conditions, because any climb event can be replaced by a "virtual" climb composed of two glide events to and from the grain boundary. In order to estimate the proximity to equilibrium, the diffusion constant for dislocation glide is measured by following the motion of dislocations over the 30-min annealing period after each increment in applied field as discussed in Sec. V.

Because bubbles are widely spaced relative to their radii in this experiment, the bubble interaction energy is well approximated by a simple dipole-dipole interaction[33] $E \propto 1/r^3$. As shown in Fig 1(b) the lattice spacings vary from 17 to 47 μm. The bubble radius is uniform from bubble to bubble, and does not vary appreciably over the range of applied fields used in this experiment (85 Oe $< H_B <$ 95 Oe), even though the density ρ varies by an order of magnitude. The distribution of bubble radii was measured following each step in H_B. The average bubble radius $r=3.26$ μm varies by less than 0.13 μm over the full range of bias field, and the measured standard deviation of the distribution of bubble radii in any single image

is ≤ 0.4 μm. The bubble radius was also observed to be independent of the coordination of the bubble in the array. The magnetic dipole moment of each bubble changes little with applied field H_B and is quite uniform from bubble to bubble, because the bubble radius changes little and the magnetization of the film is uniform. The bubble dipole moment is $\mu \cong 0.8 \times 10^{-8}$ (Gaussian units) and the bubble-bubble interaction energy is $\sim 10^7 - 10^6$ K over the range of H_B; corrections to the dipole approximation are estimated[33] to be 2% to 14%.

III. MELTING OVERVIEW

Figures 3(a)–3(f) present a series of processed images selected from a larger set to illustrate the hexatic-to-liquid melting transition as the bubble density ρ is reduced by increasing the applied bias field H_B. In these images the white squares, black squares, black circles, and white circles correspond to bubbles with four, five, seven, and eight adjacent bubbles, respectively, representing lattice disclinations. Pairs of five- and sevenfold coordinated disclinations, which corresponds to dislocations, can be easily identified at high density, and tend to orient head to tail as predicted by theory. As melting occurs these disclination pairs increase in concentration and form increasingly large transient clusters. The pairs eventually dissociate and the clusters span the system,

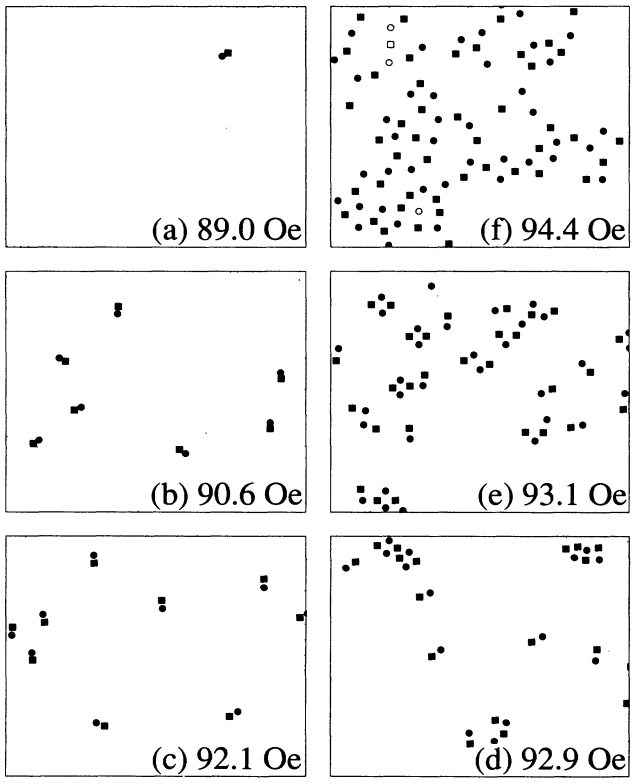

FIG. 3. Overview of the melting transition: sections of processed images at the values of the bias field H_B indicated illustrating the melting process (see text). Open squares, black squares, black circles, and open circles represent bubbles with four, five, seven, and eight adjacent bubbles in the hexagonal array, corresponding to disclinations. Black square-black circle pairs represent dislocations.

destroying orientational order. In this section we review this observed melting process, previously described in Ref. 28.

The initial array in Fig. 3(a) has extended orientational order, very low defect concentration, and low defect mobility. Here dislocations are observed to glide across $\sim 10\%$ of the field of view in the annealing time. The array in Fig. 3(a) appears crystalline, but is actually a hexatic glass with short-range translational order analogous to that of Chudnovsky[24] and of Bouchaud, Mezard, and Yedidia.[25] The dominant cause for the absence of translational order in this hexatic glass is microscopic roughness, although dislocations not included in these theories do contribute to the disruption of translational order in experiment. The bubble density ρ was reduced between Figs. 3(a) and 3(b) by breaking bubbles at uncorrelated positions distributed uniformly over the array by increasing the applied perpendicular dc bias magnetic field H_B, as described above, creating vacancies that relax into dislocations. After annealing, the result shown in Fig. 3(b) is a Halperin-Nelson hexatic[6] characterized by a gas of dislocations which limits translational order: here dislocations glide across $\sim 35\%$ of the field of view in the annealing time. Although the array is still far from equilibrium, the dislocation gas closely resembles the hexatic described by equilibrium Halperin-Nelson theory, because dislocations are created uniformly and can equilibrate locally. The hexatic in Fig. 3(c) for lower bubble density has diffusion constants similar to Fig. 3(b). In Fig. 3(d) a dramatic increase in the dislocation concentration and mobility starts to occur. Here dislocations glide across $\sim 110\%$ of the field of view in the annealing time. Dislocations begin to form transient clusters in Fig. 3(d). These clusters evolve continuously in time, as the dislocations constantly rearrange and go into and out of existence. In contrast to nuclei in first-order transitions these transient clusters do not stabilize and grow upon attaining a critical size. Time-resolved images show events corresponding to thermal excitation of virtual dislocation pairs and dislocation regrouping, combination, and separation on time scales ~ 15 s, indicating that the hexatic is near equilibrium, as discussed below. The hexatic-to-liquid transition occurs over Figs. 3(d) and 3(e). In Fig. 3(e) larger transient defect clusters form as clusters begin to join each other and percolate across the system: the cluster size is comparable to the cluster spacing. The diffusion constant for Fig. 3(e) and lower densities is large but difficult to measure, because dislocations are continually created and destroyed. Finally, in Fig. 3(f), the transient defect clusters span the system, dislocations dissociate into disclinations, orientational order diminishes, and the system is a liquid. Here isolated disclinations can be identified, and it is no longer possible to uniquely pair five- and sevenfold coordinated disclinations. At these low densities, bubbles with four and eight adjacent bubbles are also often present. Isolated clusters are no longer present in the system.

The series of measurements illustrated in Fig. 3 were repeated four times, with similar results. Neither the orientation of the bubble array in crystallites nor the location of topological defects is determined by the garnet

film or substrate, and both vary from measurement to measurement. The melting process and dynamics are observed to be qualitatively identical for all crystallites, and the measured average properties quantitatively agree. Therefore, melting driven by topological lattice defects is intrinsic to the two-dimensional magnetic bubble array.

IV. CORRELATION FUNCTIONS AND CORRELATION LENGTHS

The evolution of the bubble array through the melting transition can be characterized by the translational correlation function $G_T(r)$ and the orientational correlation function $G_\theta(r)$, which are shown in Fig. 4 for selected values of bias field H_B. The translational correlation function $G_T(r)$ was calculated from the measured bubble centers using the local Fourier component $e^{iK\cdot r}$ as the order parameter:

$$G_T(r)\langle e^{iK\cdot r'}e^{-iK\cdot(r'-r)}\rangle \ . \tag{1}$$

Here, K is the reciprocal lattice vector to the first Bragg peak in the structure factor, determined from the measured bubble centers using a discrete Fourier transform. The angle brackets represent an average over all pairs of bubbles separated by r and an angular average over the six vectors K measured from the two-dimensional structure factor. The orientational correlation function $G_\theta(r)$ was calculated from the measured bond centers and angles θ using the orientational order parameter $e^{i6\theta}$ for a hexagonal lattice:

$$G_\theta(r)=\langle e^{i6\theta(r')}e^{-i6\theta(r'-r)}\rangle \ . \tag{2}$$

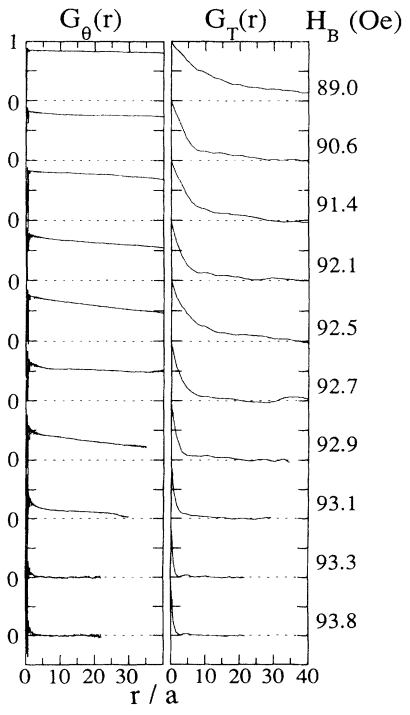

FIG. 4. Orientational correlation functions $G_\theta(r)$ and translational correlation functions $G_T(r)$ for the values of H_B indicated vs r in units of the average lattice spacing a.

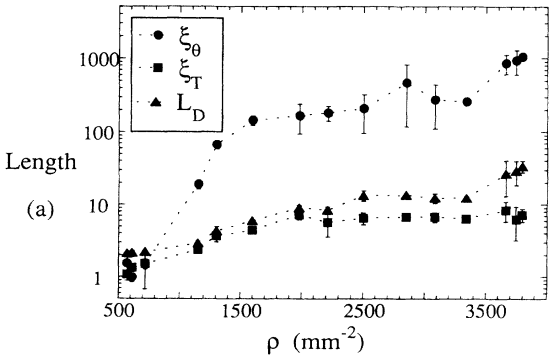

FIG. 5. Orientational correlation length ξ_θ, translational correlation length ξ_T, and average spacing between dislocations L_D, all in units of the average lattice spacing a vs bubble density ρ. For $\rho > 3500$ mm^{-2} the system is a hexatic glass, and for 1600 mm$^{-2} < \rho < 3500$ mm^{-2} a hexatic. The hexatic-to-liquid transition occurs over 1100 mm$^{-2} < \rho < 1600$ mm^{-2}, and the system is a liquid for $\rho < 1100$ mm^{-2}.

Here, the word "bond" refers to the line joining adjacent bubbles. The angle brackets represent an average over paris of bonds separated by r and an angular average over $\pi/3$ radian segments.

In Fig. 5 the correlation lengths ξ_T and ξ_θ determined from the measured translational and orientational correlation functions are shown as a function of the bubble density ρ. The translational correlation length ξ_T was determined from the width of the first Bragg peak in the angular average of the structure factor using fits to a Lorentzian line shape $S(k) \propto ((k-K)^2+\xi_T^{-2})^{-1}$, where k is the reciprocal space variable. The orientational correlation length ξ_θ was measured from exponential fits e^{-r/ξ_θ} to the orientational correlation function over $0 \le r \le 20a$, where a is the average lattice spacing. The average dislocation spacing L_D, also shown in Fig. 5, was determined from the measured dislocation concentration N_D using $L_D = (N_D)^{-1/2}$.

As shown in Figs. 4 and 5, translational order decays exponentially at all bubble densities ρ. Translational order in this system is disrupted by dislocations and by microscopic substrate roughness. Dislocations produce lattice strains which decrease as $1/r$ away from the dislocation. Microscopic roughness produces small random displacements of individual bubbles, which strain the lattice. The hexatic glass present at the highest bubble densities shown in Figs. 3–5 ($\rho \sim 3800$ mm^{-2} to 3660 mm^{-2}) has extended orientational order, but short-range translational order, as shown in Fig. 5. For these data, dislocations are far apart and large dislocation free regions exist, and dynamic observations indicate that these dislocations are relatively immobile. As shown in Fig. 5 the average dislocation spacing is $L_D \sim 30a$ at the highest bubble densities, while the translational correlation length is much shorter, $\xi_T \sim 7a$, indicating that the dominant cause for loss in translational order is microscopic roughness. This observed hexatic glass is analogous to that predicted by Chudnovsky[24] and by Bouchaud, Mezard, and Yedidia,[25]

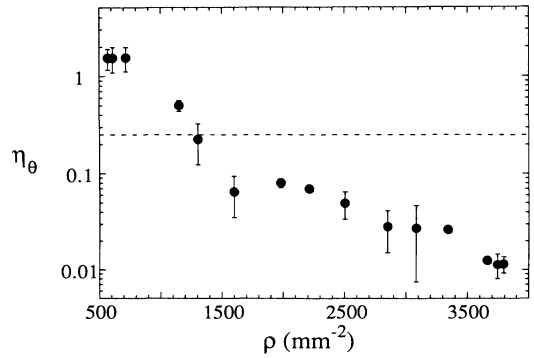

FIG. 6. Orientational exponent η_θ measured from algebraic fits $\propto r^{-\eta_\theta}$ to the orientational correlation function $G_\theta(r)$ vs bubble density ρ. The data point $\rho=1300$ mm^{-2} with $\eta_\theta=0.22\pm0.10$ at the center of the observed transition agrees well with $\eta_\theta=0.25$ (dashed line) predicted are at the hexatic-to-liquid transition by the Halperin-Nelson theory.

although dislocations are absent in the theoretical hexatic glasses. Measurements indicate that the translational correlation function of the observed hexatic glass decays as $G_T(r)\sim e^{-r^\alpha}$ with $\alpha=0.8\pm0.1$ at $\rho=3796$ mm^{-2}, $\alpha=0.7\pm0.1$ at $\rho=3746$ mm^{-2}, and $\alpha=0.8\pm0.2$ at $\rho=3661$ mm^{-2}. In comparison Chudnovsky[25] predicts $\alpha=2$, and Bouchaud, Mezard, and Yedidia[25] predict $\alpha=0.67$. We also determined the ratio $R=\xi_T^{\parallel}/\xi_T^{\perp}$ of the two extreme correlation lengths, measured from translational correlation functions $G_T(r)$ for values of r parallel to K and for r perpendicular to K. We found that $R=1.7\pm0.3$ at $\rho=3796$ mm^{-2}, $R=1.2\pm0.1$ at $\rho=3746$ mm^{-2}, and $R=1.9\pm0.8$ at $\rho=3661$ mm^{-2}. These values are close to $R=\sqrt{3}$ predicted by Chudnovsky,[24] and $R=1.67$ predicted by Bouchaud, Mezard, and Yedidia.[25]

At somewhat lower density, the array first forms a nonequilibrium Halperin-Nelson hexatic which then approaches equilibrium at lower bubble densities [$\rho\sim3660$ mm^{-2} to 1600 mm^{-2} in Figs. 3(b) and 3(c), and in Figs. 4 and 5]. In this regime the orientational correlation length is long $\xi_\theta\sim100a$, while the translational correlation length is quite short $\xi_T\sim5a$. The dislocation spacing L_D is comparable to the translational correlation length ξ_T, indicating that the dislocations account for the absence of translational order. As shown in Figs. 4 and 5, orientational order drops sharply as the hexatic-to-liquid transition occurs at lower bubble density, and the system becomes a liquid at bubble densities below 1100 mm^{-1} with short translational and orientational correlation lengths approaching one lattice spacing.

In order to characterize the decay in orientational order with bubble density ρ, we made an algebraic fit to the orientational correlation function $G_\theta(r)\propto r^{-\eta_\theta}$ over the range $0\le r\le20a$; the exponents η_θ obtained from these fits are shown in Fig. 6. For the high-density hexatic glass the exponent is quite small $\eta_\theta\sim0.01$, while for the nonequilibrium and equilibrium Halperin-Nelson hexatic the exponent is somewhat larger $\eta_\theta<0.1$. For the liquid the nominal exponent from the fit is large, $\eta_\theta>1.0$, although the actual decay is exponential. The exponent at the hexatic-to-liquid transition calculated in the equilibrium Halperin-Nelson theory is $\eta_\theta=0.25$, represented in Fig. 6 by the dotted line. The measured value $\eta_\theta=0.22\pm0.10$ at a data point $\rho=1300$ mm^{-2} at the center of the observed melting transition agrees well with the theoretical prediction as shown in Fig. 6.

V. DEFECT DYNAMICS AND THERMALIZATION

In part I (Ref. 29) we discussed measurements of the thermal properties of isolated magnetic bubbles agitated with an ac magnetic field. In this section we discuss measurements of defect dynamics and thermalization of magnetic bubble arrays, made possible by agitation with an ac magnetic field. Equilibrium is difficult to attain in many two-dimensional systems because the time required is long compared to time t_{climb} for dislocation climb, given by[9]

$$t_{\text{climb}}\sim\frac{\xi_T^2}{D_{\text{climb}}}\ , \tag{3}$$

where ξ_T is the translational correlation length of the system and D_{climb} is the diffusion constant for dislocation climb. Dislocation climb is a slow process, because it requires the absorption and emission of interstitials and vacancies, and long periods of time are typically required to attain equilibrium. Boundary conditions present a second problem in most systems because they impose external stress which deforms the lattice.

Our experiments are done within single crystallites in a polycrystalline array. The boundary condition for a crystallite is the grain boundary, which is a reservoir of dislocations surrounding the crystallite. These boundary conditions have two important consequences. The grain boundary acts to minimizes external stress on the crystallite. The grain boundary also acts as a reservoir of defects which can equilibrate with defects inside the crystallite. Because the grain boundary surrounds the crystallite, a dislocation of any orientation in the crystallite can reach the grain boundary by glide, and the time for excess dislocations to escape is given by the glide diffusion time t_{glide}:

$$t_{\text{glide}}\sim\frac{\xi_T^2}{D_{\text{glide}}}\ . \tag{4}$$

The rate for dislocation glide is typically much faster than for climb, and glide is the dominant mode of dislocation motion observed in our bubble arrays. Climb is also observed, but occurs more infrequently. However, in this system any necessary climb event is equivalent to a pair of glide events to and from the grain boundary, so that climb events are not necessary to achieve equilibrium. The equilibration time for a given type of event can be computed in principle from the nonequilibrium statistical mechanics of a gas topological defects colliding with each other and with the grain boundary.

We measured the rate of dislocation glide to estimate the proximity to equilibrium at each value of the bubble density ρ. We determined the diffusion constant D_{glide} by taking four successive images 15 s apart, and tracking the motion of each dislocation across the images. In the hex-

atic glass (for $\rho \cong 3800$ mm^{-2} to 3660 mm^{-2}) dislocations are immobile. Measurements indicate that $D_{\text{glide}} \cong 0.6$ μm^2/s to 0.8 μm^2/s, corresponding to dislocations diffusing across only $\sim 10\%$ of the field of view in the annealing time. In the nonequilibrium Halperin-Nelson hexatic (for $\rho \cong 3340$ mm^{-2} to 1980 mm^{-2}) the diffusion constant jumps to $D_{\text{glide}} \cong 4$ μm^2/s to 6 μm^2/s and the dislocations become somewhat mobile. Here dislocations glide across $\sim 35\%$ of the field of view in the annealing time. As the equilibrium hexatic is approached the diffusion constant begins to rise: for $\rho = 1600$ mm^{-2} ($H_B = 92.7$ Oe) we measure the glide diffusion constant to be $D_{\text{glide}} \cong 11$ μm^2/s and dislocations diffuse across $\sim 50\%$ the field of view in the annealing time. At lower densities ($\rho < 1600$ mm^{-2}) the diffusion constant increases sharply to $D_{\text{glide}} > 40$ μm^2/s. This rise in dislocation mobility is accompanied by a dramatic increase in dislocation concentration as described below. As a result dislocation glide and regroup continuously producing rapidly evolving defect dynamics, which makes an accurate measurement of D_{glide} difficult.

Figure 7 illustrates the rapid and complex dislocation dynamics observed near the hexatic-to-liquid transition. Figures 7(a)–7(d) show four sequential images of the array taken 15 s apart at $\rho = 1300$ mm^{-2} ($H_B = 92.9$ Oe). Figure 7(e) shows the flow diagram for Figs. 7(a)–7(d):

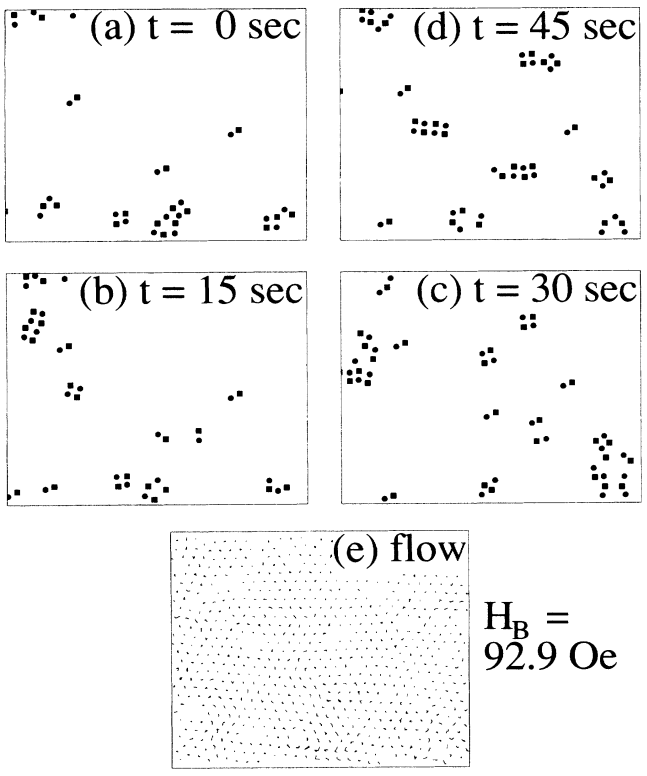

FIG. 7. (a)–(d) Four images taken 15 sec apart illustrate defect dynamics near the melting transition. Dynamics shown include thermal excitations of virtual dislocation pairs, and defect combinations and separations via dislocation glide (see text). (e) Bubble motion determined from (a)–(d): each line represents the motion of one bubble over the 45-sec period.

each line in Fig. 7(e) represents the motion of a bubble over the 45-s period. Figure 7(e) shows that the dislocation production and dynamics illustrated in Figs. 7(a)–7(d) is due to bubble motion in the array. The dislocation dynamics illustrated in Figs. 7(a)–7(d) are described below in terms of a few types of simple events.

The simplest defect cluster observed in Figs. 7(a)–7(d) is a virtual dislocation pair, which is composed of two dislocations with antiparallel Burger's vectors and common glide planes as described in Ref. 29. Virtual pairs are easy to locate in Figs. 7(a)–7(d): they correspond to two fivefold disclinations (two black squares) and two sevenfold disclinations (two black circles) arranged in a quadrupole. These virtual pairs are excited thermally from a defect-free hexagonal array by a slight distortion of the array. They annihilate in a similar manner when the two dislocations glide onto one another and combine to produce a defect-free hexagonal array. These thermal excitations and annihilations account for the appearing and disappearing virtual pairs in Figs. 7(a)–7(d). Near the hexatic-to-liquid transition, these virtual pairs create an additional source of dislocation production and destruction in the equilibrium array.

When gliding dislocations collide they can combine into fewer dislocations. For example, two dislocations whose Burger's vectors are not parallel and whose glide planes are different can glide onto one another to form one dislocation with a glide plane along the third direction of the hexagonal lattice. One such event occurs between Figs. 7(a)–7(b), in the lower right-hand corner of the image: one of the dislocations in the virtual pair combines with the third dislocation nearby. Dislocations can also separate into more dislocations. A gliding dislocation can split into two other dislocations, just as two dislocations can combine into one. An event of this type occurs between Figs. 7(a) and 7(b), just below the center of the image. We also observe recombination events where the disclinations from two colliding dislocations swap partners and regroup into two new dislocations.

VI. DEFECT CONCENTRATIONS AND DISTRIBUTIONS

The hexatic-to-liquid transition in this system is driven by topological defects as described above, in agreement with the equilibrium Halperin-Nelson theory.[6–9] In this section we present measurements of concentrations and distributions of topological defects as a function of the bubble density ρ. We observe that the characteristic signature of the hexatic-to-liquid transition is a dramatic increase in defect concentration and a sudden broadening of the defect distribution. In the hexatic glass the measured defect concentration after 30 min of annealing is observed to be directly proportional to the number of defects introduced before annealing.

In this experiment the decrease in bubble density occurs via bubble-collapse events distributed uniformly over the array. The bubble-collapse events generate vacancies which relax into dislocations. We allow the array to anneal for 30 min, and then record images and make measurements. In order to estimate the extent of equilibration that occurs in the 30-min annealing period we

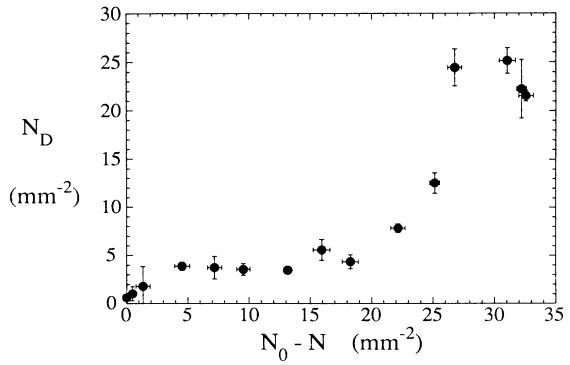

FIG. 8. The measured disclination concentration N_D after annealing (N_0-N) a measure of the number of defects introduced prior to annealing, where N_0 is the number of bubbles present at the start of the experiment and N is the number present at the bias field at which the measurement was made (see text).

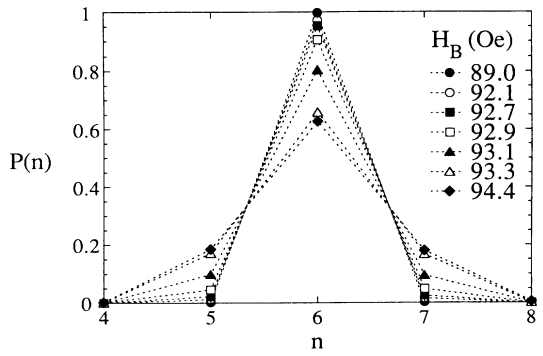

FIG. 9. Probability $P(n)$ of a bubble having n adjacent bubbles vs n, for the values of H_B indicated. Initially the distribution is sharply peaked at $n=6$. It broadens symmetrically at the melting transition.

compare the defect concentrations before and after annealing. In Fig. 8 we plot N_D the measured disclination concentration after annealing versus (N_0-N) a measure of the number of defects introduced prior to annealing, where N_0 is the number of bubbles present at the start of the experiment and N is the number present at the bias field at which the measurement was made.

Figure 8 shows that in the hexatic glass $[(N_0-N)<500\ mm^{-2}]$ the number of defects present after annealing is directly proportional to the number introduced prior to annealing. This implies that the defects in the hexatic glass do not equilibrate in the annealing period, which is consistent with measured values of D_{glide} presented above. In Fig. 8, after this initial linear increase we see a change in slope at $(N_0-N)\cong 500\ mm^{-2}$. In the hexatic phase $[(N_0-N)=500\ mm^{-2}$ to $2000\ mm^{-2}]$ the slope is essentially zero, and the number of defects in the annealed array is independent of the number of defects introduced by incrementing H_B. Now many of the dislocations introduced prior to annealing escape to the grain boundary or annihilate each other during the annealing period. However measured values of D_{glide} presented above indicate that 30 min is not adequate for complete equilibration in the high density Halperin-Nelson hexatic. At these densities the extent of equilibration indicated by Fig. 8 could be because dislocations are introduced uniformly and can equilibrate locally. At lower densities, Fig. 8 shows a sharp rise in the number of disclinations in the annealed array near $(N_0-N)=2600\ mm^{-2}$, which corresponds to $H_B=92.9$ Oe and $\rho=1300\ mm^{-2}$. This dramatic increase, accompanied by the thermal excitation of virtual dislocation pairs, is a characteristic signature of the hexatic-to-liquid transition. Above this sharp increase, for $(N_0-N)>3000\ mm^{-2}$, the system is a liquid. The drop in defect concentration at very large values of (N_0-N) is an experimental artifact due to a decrease in the total number of bubbles in an image.

To study the evolution of topological disorder we measured distributions of lattice defects in the system. In Fig. 9 the probability of finding a bubble with n adjacent bubbles is plotted versus n, for a range of densities ρ. Note that $n=6$ for all bubbles in a defect-free hexagonal array, and this value of n does not represent a lattice defect. The first distribution ($H_B=89.0$ Oe) shown in Fig. 9 is a typical distribution observed at hexatic glass densities. Here almost all the bubbles are sixfold coordinated, indicating low topological disorder and defect concentration. The second distribution shown ($H_B=92.1$ Oe) is typically observed at Halperin-Nelson hexatic densities. In this hexatic phase the distribution broadens to include a few five- and sevenfold coordinated bubbles, corresponding in Fig. 3 to a gas of dislocations. The next three distributions in Fig. 9 show the array near the transition ($H_B=92.7$ Oe, 92.9 Oe, 93.1 Oe). The distribution widens sharply at the hexatic-to-liquid transition taking the system from sharp hexatic distributions to broad liquid distributions. In the liquid phase ($H_B=93.3$ Oe, 93.4 Oe) the distribution includes many more five- and sevenfold coordinated bubbles, and a few four- and eightfold coordinated bubbles, all corresponding to free disclinations. In the liquid the distribution of disclinations is not observed to vary appreciably with bubble density.

Figure 9 shows that the widening of the distribution at the hexatic-to-liquid transition occurs symmetrically around $n=6$. We define the topological charge e of a bubble with n adjacent bubbles by $e=(n-6)$. By this definition sevenfold (eightfold) coordinated disclinations have a topological charge of $+1$ $(+2)$ while fivefold (fourfold) coordinated disclinations have a topological charge of -1 (-2). The symmetrical broadening of the distributions implies that the net sum of topological charges in the system at any value of the bias field H_B equals zero. As expected, topological charge neutrality, an assumption made in the Halperin-Nelson theory of two-dimensional melting,[6-9] is preserved. Observations of the array indicate that topological charge neutrality is preserved locally as well, over areas with linear dimensions of a few lattice spacings.

VII. PHENOMENOLOGICAL DESCRIPTIONS OF MELTING

Phenomenological approaches such as the use of the Lindemann criterion are very useful for characterizing phase transitions in three dimensions. According to the Lindemann criterion, melting occurs in three-dimensional systems when the mean-square displacements of particles from their equilibrium position in a lattice $\langle u(R)^2\rangle \cong 0.1a$, where a is the average lattice spacing. Unfortunately $\langle u(R)^2\rangle$ diverges with system size in two dimensions. However, the mean square of the difference between displacements of adjacent bubbles $\langle (u(R+a)-u(R))^2\rangle$ is finite in two dimensions, and therefore a useful phenomenological measure of melting.[34] Here, $u(R)$ is the displacement of a bubble from its position R in the ideal lattice, or $r=(u(R)+R)$ is the actual position of the bubble in the array. The quantity a, the lattice spacing of the ideal lattice, equals the average of the separations α between adjacent bubbles in the array.

The distributions $P(\alpha)$ of adjacent bubble separations α varies with bias field H_B as shown in Fig. 10. The distribution is sharply peaked for the hexatic glass and the hexatic, as shown by the curves $H_B=88.9$ Oe to 92.5 Oe in Fig. 10. The distribution broadens at the hexatic-to-liquid transition, as shown by $H_B=92.7$ Oe to 93.1 Oe in Fig. 10. For the liquid the distribution remains broad, as shown by $H_B=93.3$ Oe and 93.8 Oe in Fig. 10.

In order to study the broadening of this distribution $P(\alpha)$ at the transition, we measured the widths of the distribution as a function of H_B. The result of this measurement is standard deviations W of the distributions $P(\alpha)$ of α, plotted as a function of H_B in Fig. 11. Figure 11 shows that at the phase transition $W\cong 0.1a$. As Fig. 11 shows $W\cong 0.06a$ in the hexatic phases, for $H_B<92.5$ Oe. At the hexatic-to-liquid phase transition W increases sharply, between $H_B=92.5$ Oe and 93.1 Oe. For the liquid phase $W>0.13a$, for $H_B>93.1$ Oe. Note that $W^2=\langle(\alpha-a)^2\rangle$ by definition, and it is straightforward to show that $\langle(\alpha-a)^2\rangle=\langle(u(R+a)-u(R))^2\rangle$. Therefore, the hexatic-to-liquid transition in two-dimensional magnetic bubble arrays occurs when the root-mean

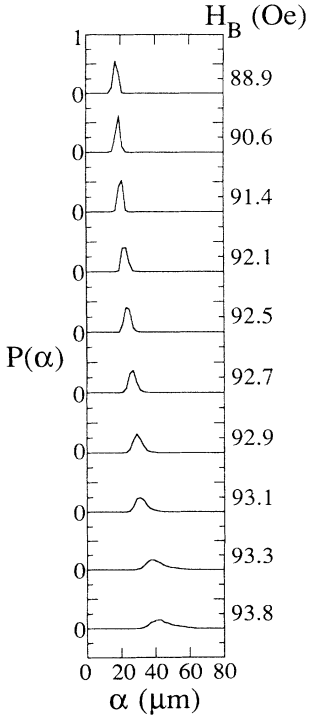

FIG. 10. Probability distributions $P(\alpha)$ of lattice spacings measured using Voronoi construction vs spacings α for the values of H_B indicated. Initially the distribution is sharply peaked. It broadens at the melting transition.

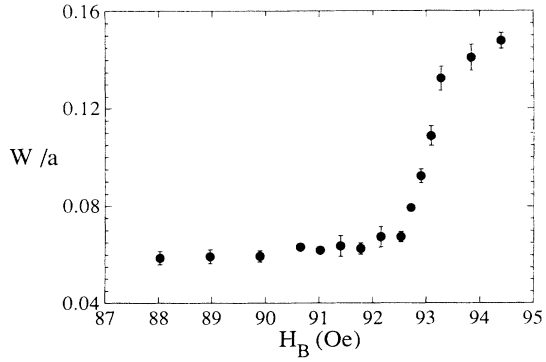

FIG. 11. Standard deviations W of the distributions $P(\alpha)$ shown in Fig. 10 vs the bias field H_B. W is a useful phenomenological melting criterion in two dimensions (see text): at the transition $W\cong 0.1a$.

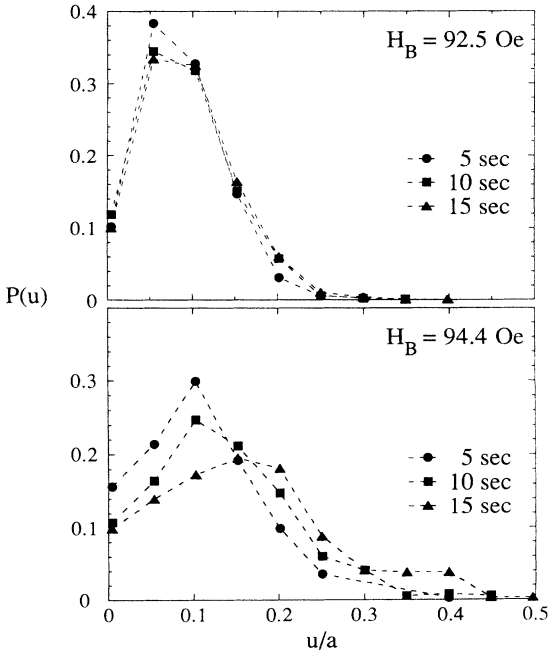

FIG. 12. Probability $P(u)$ of a bubble moving a distance u in a constant interval of time vs u. Measurement for time intervals of 5, 10, and 15 s are shown. (a) A typical distribution observed at hexatic densities indicates constrained bubble motion. (b) A typical distribution observed at liquid densities indicates diffusive bubble motion.

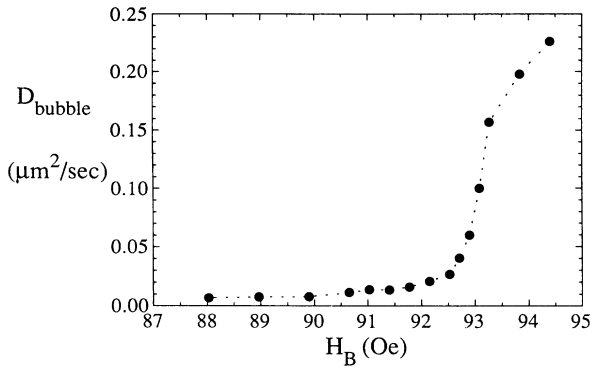

FIG. 13. Bubble diffusion constant D_{bubble} vs bias field H_B. At the melting transition D_{bubble} increases rapidly as the bubble motion goes from being constrained to being diffusive.

square of the difference between displacements of adjacent bubbles $(\langle (u(R+a)-u(R))^2 \rangle)^{1/2} \cong 0.1a$. This measured behavior agrees well with that found in the numerical simulations described in Ref. 34, indicating that the modified Lindemann criterion is useful for characterizing melting transitions in two dimensions and for making comparisons between different systems.

Our observations also indicate that at the hexatic-to-liquid transition the motion of bubbles in the array goes from constrained in the hexatic phase to diffusive in the liquid phase. To study the bubble motion we determined distributions $P(u)$ of measured bubble displacements u over constant time intervals $t=5$, 10, and 15 s. Figures 12(a) and 12(b) illustrate typical distributions observed in the hexatic and liquid phases respectively. In Fig. 12(a), $P(u)$ does not vary appreciably with time, indicating constrained bubble motion. In Fig. 12(b), $P(u)$ widens as a function of time, and its mean value moves to larger u. Figure 12(b) shows that the bubble motion is diffusive in the liquid.

We determined a diffusion constant for bubble motion D_{bubble} from the measured bubble displacements. In Fig. 13 we plot this diffusion constant D_{bubble} versus the bias field H_B. In the hexatic glass ($H_B=88.0$ Oe to 89.9 Oe) the bubble motion is constrained with $D_{bubble} \cong 0.005$ $\mu m^2/s$, and bubbles are trapped by the array. In the Halperin-Nelson hexatic ($H_B=90.6$ Oe to 92.5 Oe), bubble motion is still constrained with $D_{bubble} \cong 0.01$ $\mu m^2/s$. At the hexatic-to-liquid transition the diffusion constant increases rapidly over $H_B=92.7$ Oe to 93.1 Oe, with $D_{bubble} \cong 0.1$ $\mu m^2/s$ at the center of the transition. In the liquid phase ($H_B=93.3$ Oe to 94.4 Oe) bubble motion is diffusive with $D_{bubble} > 0.15$ $\mu m^2/s$.

VIII. MELTING IN A GRADIENT MAGNETIC FIELD

Melting in two dimensions has generated controversy in the past because competing theories have very different predictions for the order of the phase transition.[1-3] To test whether the hexatic-to-liquid transition we observe is first order we performed the melting experiment in the presence of a small linear gradient in the bias magnetic field. The gradient field produces a gradient in the bubble density across an image, with a range spanning the transition. The presence of a melting front or phase separation would be the signature of a first-order transition, while a continuous coarsening of the array would signal a continuous phase transition.

In this experiment the annealed bubble array was placed in a linearly varying perpendicular magnetic field gradient of magnitude 0.005 Oe/μm. This gradient field adds to the applied perpendicular bias magnetic field H_B. Then H_B was increased slowly to 90.8 Oe, and the array was allowed to anneal for 30 min in a 6.6-Oe peak-to-peak, 40-Hz perpendicular ac field. This ac field enables the array to respond to the pressure gradient produced by the gradient magnetic field, resulting in an equilibrium bubble density gradient across the image. The charge-coupled-device camera was set up so that the center of the image obtained coincided with the center of the magnetic field gradient, where the magnetic field due to the gradient is zero. Image of size 1460×1095 μm^2 were recorded. The gradient field produced a continuous range of bias fields between 87.1 and 94.4 Oe across the image, and the resulting bubble densities spanning the image ranged continuously from hexatic-to-liquid values.

A section of a typical image obtained is shown in Fig. 14. The lattice spacing ranges from ~ 20 μm on the left, corresponding to hexatic densities, to ~ 46 μm on the right, corresponding to liquid densities, over a distance 1370 μm. Melting shown in Fig. 14 occurs via a process similar to that in Fig. 3. A typical large-angle grain boundary, which is the boundary condition on the crystallite, is shown for comparison in the lower left-hand corner of Fig. 14. We do not observe such large-angle grain-boundary structures inside the crystallite at any density. We do not observe an interface at the transition separating the hexatic and liquid phases. We also do not observe phase separation or two-phase coexistence. We observe a gradual coarsening of the array from left to

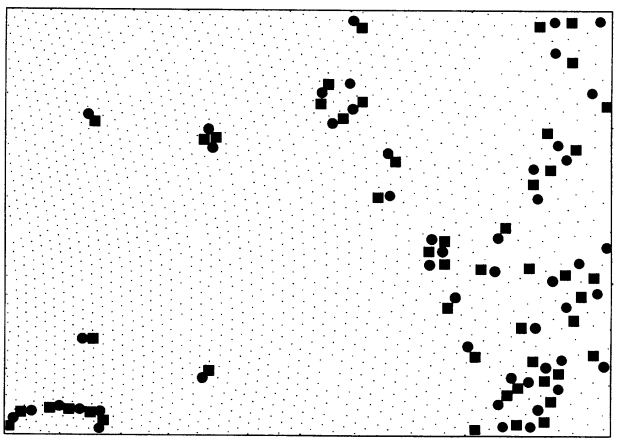

FIG. 14. Melting in the presence of a linear gradient in the vertical magnetic field indicates a continuous transition (see text). The field increases by 7 Oe from left to right over a distance 1370 μm, and produces a gradient in the bubble density. Lattice spacings range from 20 μm at the left to 46 μm at the right, spanning the melting transition.

right. The dislocations do cluster but the clusters rearrange constantly and evolve continuously. These transient clusters do not nucleate and grow upon attaining a critical size like those in first-order transitions. Our observations therefore indicate that the hexatic-to-liquid transition is continuous. This is consistent with the measured gradual decrease in the bubble density ρ as a function of H_B in the original experiment, shown in Fig. 1(a).

To confirm that the continuous transition we observed was not a result of an equilibration problem, we repeated the gradient experiment allowing the array to anneal for ~ 2000 min (14 days) in the ac field.[35] Our observations were the same as above, confirming that the transition is continuous. We estimate that in the 14-day annealing period the dislocations in the hexatic glass, hexatic, and liquid can glide across $\sim 270\%$, $\sim 730\%$, and $\sim 2900\%$ of the field of view, respectively, or across $\sim 50\%$, $\sim 115\%$, and $\sim 260\%$ of the crystallite (size $\sim 10^5$ bubbles), respectively. This system is clocked at the ac field frequency of 40 Hz which implied that the array anneals for $\sim 10^6$ ac cycles. The annealing time equals $\sim 3\times 10^5$ τ, $\sim 1\times 10^5$ τ, and $\sim 6\times 10^5$ τ for the hexatic glass, hexatic, and liquid phases, respectively, where τ is the average diffusion time for a dislocation to move one lattice spacing.

IX. CONCLUSIONS

In this paper we have examined in detail the structural and topological changes that occur in magnetic bubble arrays undergoing the process of two-dimensional melting. The results agree with the predictions of the equilibrium Kosterlitz-Thouless-Halperin-Nelson-Young theory for the hexatic and liquid phases, and for the hexatic-to-liquid transition. We see transient cluster formation in the hexatic phase. These clusters grow in size and percolate across the system as the bubble density decreases. When the clusters span the system, we observe a liquid with free disclinations. The diffusion constant for dislocation glide and the defect dynamics indicate that the system is at equilibrium near the transition. At the transition, virtual dislocation pairs are thermally excited and, as a result, the defect concentration shows a dramatic increase and the distribution of defects broadens suddenly. The system maintains topological charge neutrality at all densities. Observations in the presence of a gradient in the bubble density indicate that the transition is continuous. The melting transition is described well by a phenomenological criterion analogous to the Lindemann criterion: melting occurs when the root-mean square of the difference between the displacements of adjacent bubbles equals $\sim 10\%$ of the average spacing between bubbles.

Because of the presence of microscopic disorder due to substrate roughness in the sample, translational order is short ranged for all densities in this system. Therefore at high bubble densities, away from the transition, we see a hexatic glass with low defect concentration and low defect mobility, having short-range translational order and long-range orientational order. A hexatic-to-crystal transition and a crystal phase that has algebraically decaying quasi-long-range translational order is not seen.

The bubble-bubble interaction in this system is approximated well by a simple dipolar repulsion ($1/r^3$). For an interaction of the form $1/r^n$ one can show that the partition function depends only on the ratio Γ between the average interaction energy per particle and the thermal energy, and this ratio can be used to estimate the location of the system in the phase diagram.[15] At the hexatic-to-liquid transition we determined this ratio $\Gamma_c=(\mu^2/a^3)/k_BT$ to be ~ 30, using measured values for μ, a, and T from Ref. 29 and this paper. This is close to the value of $\Gamma_c=59-65$ reported in numerical simulations of systems with dipolar repulsion.[15,16] Our results do not agree with the conclusions reported in these numerical simulations, for which first-order transitions are obtained.

Two-dimensional arrays of magnetic bubbles provide a means to study the melting process and the resulting phases dynamically. The properties of this system and the physical processes involved are similar in some ways to the vortex arrays in type-II superconductors, and a considerable amount of theory that has been worked out for superconductors is applicable here. Although static images of the vortex arrays have been observed,[26,27] dynamical properties are difficult to study using existing techniques. Therefore results from magnetic-bubble arrays might help us to understand the basic dynamical properties of vortex arrays.

ACKNOWLEDGMENTS

We are grateful to Roger Belt and the Airtron Division of Litton Industries for the garnet films. We thank David Nelson, Daniel Fisher, Ken Babcock, Jonathan Selinger, and Jed Dempsey for helpful conversations, and the Condensed Matter Theory Group and the Robotics Group at Harvard University for use of their computers. This work was supported by the Office of Naval Research under Grant Nos. N00014-89-J-1592 and N00014-89-J-1023.

[1]K. J. Strandburg, Rev. Mod. Phys. **60**, 161 (1988).
[2]*Ordering in Two Dimensions*, edited by S. K. Sinha (North-Holland, Amsterdam, 1980).
[3]D. R. Nelson, in *Phase Transitions and Critical Phenomena*, edited by C. Domb and J. L. Lebowitz (Academic, London, 1983), Vol. 7.
[4]N. D. Mermin, Phys. Rev. **176**, 250 (1968).
[5]J. M. Kosterlitz and D. J. Thouless, J. Phys. C **6**, 1181 (1973).
[6]B. I. Halperin and David R. Nelson, Phys. Rev. Lett. **41**, 121 (1978).
[7]David R. Nelson and B. I. Halperin, Phys. Rev. B **19**, 2457 (1979).
[8]D. R. Nelson, Phys. Rev. B **26**, 269 (1982).
[9]A. P. Young, Phys. Rev. B **19**, 1855 (1979).
[10]Daniel S. Fisher, B. I. Halperin, and R. Morf, Phys. Rev. B **20**, 4692 (1979).
[11]T. V. Ramakrishnan, Phys. Rev. Lett. **48**, 541 (1982).
[12]S. T. Chui, Phys. Rev. Lett. **48**, 933 (1982).
[13]H. Kleinert, Phys. Lett. **95A**, 381 (1983).
[14]B. Joos and M. S. Duesbery, Phys. Rev. Lett. **55**, 1997 (1985).

[15]R. K. Kalia and P. Vashishta, J. Phys. C **14**, L643 (1981).
[16]V. M. Bedanov, G. V. Gadiyak, and Yu. E. Lozovik, Phys. Lett. **92A**, 400 (1982).
[17]D. R. Nelson, M. Rubinstein, and F. Spaepen, Philos. Mag. A **46**, 105 (1982).
[18]C. A. Murray and D. H. Van Winkle, Phys. Rev. Lett. **58**, 1200 (1987).
[19]C. A. Murray and R. A. Wenk, Phys. Rev. Lett. **62**, 1643 (1989).
[20]C. A. Murray, W. O. Spenger, and R. A. Wenk, Phys. Rev. B **42**, 688 (1990).
[21]Y. Yang, A. J. Armstrong, R. C. Mockler, and W. J. O'Sullivan, Phys. Rev. Lett. **62**, 2401 (1989).
[22]G. Helgesen and A. T. Skjeltorp, Physica A **170**, 488 (1991).
[23]A. I. Larkin and Yu. N. Ovchinnikov, J. Low Temp. Phys. **34**, 409 (1979).
[24]E. M. Chudnovsky, Phys. Rev. B **40**, 11 355 (1989).
[25]J. P. Bouchaud, M. Mezard, and J. S. Yedidia, Phys. Rev. Lett. **67**, 3840 (1991).
[26]C. A. Murray, P. L. Gammel, D. J. Bishop, D. B. Mitzi, and A. Kapitulnik, Phys. Rev. Lett. **64**, 2312 (1990).
[27]D. G. Grier, C. A. Murray, C. A. Bolle, P. L. Gammel, D. J. Bishop, D. B. Mitzi, and A. Kapitulnik, Phys. Rev. Lett. **66**, 2270 (1991).
[28]R. Seshadri and R. M. Westervelt, Phys. Rev. Lett. **66**, 2774 (1991).
[29]R. Seshadri and R. M. Westervelt, preceding paper, Phys. Rev. B **46**, 5142 (1992).
[30]A. H. Eschenfelder, *Magnetic Bubble Technology* (Springer-Verlag, New York, 1981).
[31]A. P. Malozemoff and J. C. Slonczweski, *Magnetic Domain Walls in Bubble Materials* (Academic, New York, 1979).
[32]R. F. Belt and J. B. Ings, SPIE J. **753**, 142 (1987).
[33]J. A. Cape and G. W. Lehman, J. Appl. Phys. **42**, 5732 (1971).
[34]V. M. Bedanov, G. V. Gadiyak, and Yu. E. Lozovik, Phys. Lett. **109A**, 289 (1985).
[35]R. Seshadri and R. M. Westervelt, in *Proceedings of Symposium O on Complex Fluids,* edited by E. Sirota, Materials Research Society Fall Meeting, 1991 (Materials Research Society, Pittsburgh, 1992).